

Vapor phase synthesis of organometal halide perovskite nanowires for tunable room-temperature nanolasers

Xing, Jun; Liu, Xin Feng; Zhang, Qing; Ha, Son Tung; Yuan, Yan Wen; Shen, Chao; Sum, Tze Chien; Xiong, Qihua

2015

Xing, J., Liu, X. F., Zhang, Q., Ha, S. T., Yuan, Y. W., Shen, C., . . . Xiong, Q. (2015). Vapor phase synthesis of organometal halide perovskite nanowires for tunable room-temperature nanolasers. *Nano Letters*, 15(7), 4571-4577. doi:10.1021/acs.nanolett.5b01166

<https://hdl.handle.net/10356/140368>

<https://doi.org/10.1021/acs.nanolett.5b01166>

This document is the Accepted Manuscript version of a Published Work that appeared in final form in *Nano Letters*, copyright © American Chemical Society after peer review and technical editing by the publisher. To access the final edited and published work see <https://doi.org/10.1021/acs.nanolett.5b01166>

Downloaded on 09 Apr 2024 23:56:44 SGT

Vapor Phase Synthesis of Organometal Halide Perovskite Nanowires for Tunable Room-Temperature Nanolasers

*Jun Xing,[†] Xin Feng Liu,^{†,‡} Qing Zhang,[†] Son Tung Ha,[†] Yan Wen Yuan,[†] Chao Shen,[†]
Tze Chien Sum,^{†,‡,§} and Qihua Xiong^{*,†,§,¶}*

[†] Division of Physics and Applied Physics, School of Physical and Mathematical Sciences,
Nanyang Technological University, Singapore 637371

[‡] Energy Research Institute @ NTU (ERI@N), Nanyang Technological University, 50
Nanyang Drive, Singapore 637553

[§] Singapore-Berkeley Research Initiative for Sustainable Energy, 1 Create Way,
Singapore 138602

[¶] NOVITAS, Nanoelectronics Centre of Excellence, School of Electrical and Electronic
Engineering, Nanyang Technological University, Singapore 639798

*To whom correspondence should be addressed. Email address: Qihua@ntu.edu.sg

ABSTRACT

Semiconductor nanowires have been received considerable attention in the past decade driven by both unprecedented physics derived from the quantum size effect and strong isotropy, and advanced applications as potential building blocks for nanoscale electronics and optoelectronic devices. Recently, organic-inorganic hybrid perovskites have been shown to exhibit high optical absorption coefficient, optimal direct band gap and long electron/hole diffusion lengths, leading to high performance photovoltaic devices. Herein, we present the vapor phase synthesis free-standing $\text{CH}_3\text{NH}_3\text{PbI}_3$, $\text{CH}_3\text{NH}_3\text{PbBr}_3$ and $\text{CH}_3\text{NH}_3\text{PbI}_x\text{Cl}_{3-x}$ perovskite nanowires with high crystallinity. These rectangular cross-sectional perovskite nanowires have good optical properties and long electron hole diffusion length, which ensure adequate gain and efficient optical feedback. Indeed, we have demonstrated optical-pumped room-temperature $\text{CH}_3\text{NH}_3\text{PbI}_3$ nanowire lasers with near-infrared wavelength of 777 nm, low threshold of $11 \mu\text{J}/\text{cm}^2$ and a quality factor as high as 405. Our research advocates the promise of optoelectronic devices based on organic-inorganic perovskite nanowires.

KEYWORDS: Organic-inorganic perovskites, nanowire, photoluminescence spectroscopy, nanolasers

Organic-inorganic hybrid perovskites, the structural analogues of calcium titanium oxide crystal, have been widely studied due to their unique structure of alternating stacking sheet of organic and inorganic components.¹⁻³ Recently, considerable progress has shown that those perovskites exhibit high optical absorption coefficient, optimal direct band gap and long electron/hole diffusion lengths ranging from 100 nm to 175 μm , which underpin the increasingly high performance in solar cells.⁴⁻⁷ Specifically, the lead halide perovskite $\text{CH}_3\text{NH}_3\text{PbX}_3$ ($\text{X} = \text{Cl}, \text{Br}$ and I) thin film solar cells have reached a record-high efficiency of 20.1% in the past five years.⁸⁻¹³ Furthermore, the good optical and electrical transport properties of the organic-inorganic perovskites make them also suitable for other optical, electronic and opto-electronic devices, such as light-emitting diodes, laser, photodetectors and field-effect transistors.¹⁴⁻²² In general, these applications are largely determined by the crystalline quality and the structure of the materials. Perovskites with reduced dimensionality, for instance, two-dimensional crystals, have shown excellent optical properties leading to sufficient gain towards whispering gallery mode lasing.¹⁵ One dimensional nanowires synthesized by wet chemistry have also attracted some attention in solar cells and photodetectors.^{20, 23} Compared to polycrystalline thin film, low-dimensional layered crystals or nanowires exhibit higher crystalline quality thus longer carrier diffusion length, larger gain for lower threshold applications. Therefore, they are expected to play an important role as potential building blocks for the nanoscale optical, electronic and optoelectronic devices in future based on the emergent perovskite materials.

Herein, we report the synthesis of high crystalline quality $\text{CH}_3\text{NH}_3\text{PbI}_3$ nanowires with rectangular block morphology and length up to 20 μm by a two-step vapor phase method,

using PbI_2 and $\text{CH}_3\text{NH}_3\text{I}$ as precursors. Temperature dependent photoluminescence (PL) spectroscopy on individual nanowires is conducted to investigate the optical properties. The high quality $\text{CH}_3\text{NH}_3\text{PbI}_3$ nanowire constitute a built-in Fabry-Pérot microresonator as such we have demonstrated the strong optical-pumped room-temperature lasing with near-infrared wavelength of 777 nm, low threshold of $11 \mu\text{J}/\text{cm}^2$ and a quality factor as high as 405. Here, the threshold is nearly 4 times lower than that of the $\text{CH}_3\text{NH}_3\text{PbI}_3$ nanoplates in our previous report.¹⁵ By replacing $\text{CH}_3\text{NH}_3\text{I}$ with $\text{CH}_3\text{NH}_3\text{Br}$ or $\text{CH}_3\text{NH}_3\text{Cl}$, we can tune the lasing wavelength from 777 nm to 551 and 744 nm, respectively.

The perovskite nanowires are synthesized by a two-step vapor phase synthesis method. Briefly, PbI_2 nanowires were first synthesized on silicon oxide substrates by chemical vapor deposition (CVD) method, with the central zone temperature of 380 °C and substrates mounted ~12 cm downstream of the furnace. Consequently, the conversion of PbI_2 into halide perovskite through a gas-solid hetero-phase reaction with ammonium halide molecules (see Methods).²⁴ Figure 1a and S1a are the scanning electron microscopy (SEM) images of the as-grown PbI_2 on silicon substrate, illustrating that PbI_2 nanowires and bulk crystals are simultaneously grown on the silicon oxide surface. However, the nanowire morphology is dominant. Further analysis (Figure S1b-d) suggests that the PbI_2 nanowires grew vertically on silicon substrate and exhibit a rectangular or nearly square cross section with the aspect ratio ranging from 1 to 20. To obtain high density and uniform PbI_2 nanowires laid down on substrates for optical studies, a dry transfer method was used to separate the nanowire from the growth silicon substrate. We put another new silicon substrate on the top of the substrate grown PbI_2 ,

then slightly pressed it from top and finally separated two silicon wafers. According to optical microscopy observation (Figure S2a), we confirm that only PbI_2 nanowires are transferred onto silicon wafer. That is probably because of the intermolecular forces between the substrates and the flat PbI_2 nanowire surfaces. This dry transfer process can be applied to other planar substrates, such as quartz, indium tin oxide and polymer substrates, which eliminates the common dispersion in polar solutions that is not compatible with PbI_2 and reduce the quality of the subsequent product of $\text{CH}_3\text{NH}_3\text{PbI}_3$ perovskites.

Transmission electron microscopy (TEM) was used to further characterize the crystalline structure of the as-synthesized PbI_2 nanowire. As shown in Figure 2a, the nanowire has a uniform contrast, confirming that the rectangular structure of PbI_2 nanowire. The high-resolution TEM (HRTEM) image (Figure 2b) exhibits clear fringes parallel with spacing of 0.394 and 0.226 nm, which are corresponding to $(1\bar{2}10)$ and $(10\bar{1}0)$ lattice spacing of hexagonal PbI_2 crystal, respectively. Based on the observed fringes along the three directions, the white hexagon drawn in the Figure 2b shows the six relevant crystal facet being perpendicular to c axis of the PbI_2 crystal. The lattice fringe can be identified continuously across the entire surface, indicating that the PbI_2 nanowire has single-crystalline characteristic. Furthermore, the single crystalline character of the PbI_2 nanowire can also be predicated from the selected area electron diffraction (SAED) pattern in inset of Figure 2a. According to analysis of SAED result, it can be concluded that the PbI_2 nanowire grow predominantly along the $[010]$ direction and closed by the (0001) and $(000\bar{1})$ planes on the top and bottom sides. This is also consistent with the high-resolution TEM image (Figure 2b) that clearly shows the $(1\bar{2}10)$ lattice planes

perpendicular to the nanowire growth direction. It can be seen that the SAED patterns show slight elongation of the diffraction spots along [010] direction. That might be caused by the lattice distortion forming during the organic molecular inserting into the lattice of PbI_2 crystal.

$\text{CH}_3\text{NH}_3\text{PbI}_3$ perovskite nanowires were formed through intercalating the $\text{CH}_3\text{NH}_3\text{I}$ molecular into the interval sites of PbI_6 octahedrons layers. After conversion, the geometry of $\text{CH}_3\text{NH}_3\text{PbI}_3$ perovskite is still maintained as nanowire as displayed in SEM images (Figure 1c and d). The difference in color of the perovskite nanowires in optical microscopy image is attributed to the different interference in the $\text{CH}_3\text{NH}_3\text{PbI}_3$ nanowire with different thickness (more pronounced in Figure 1b), which has been confirmed by atomic force microscopy (AFM). However, the surface of $\text{CH}_3\text{NH}_3\text{PbI}_3$ nanowires become rough compared to that of the PbI_2 nanowires. AFM topography also indicates a relatively rough surface of the $\text{CH}_3\text{NH}_3\text{PbI}_3$ nanowires (Figure 1e). Additional structural characterization of the $\text{CH}_3\text{NH}_3\text{PbI}_3$ nanowires was carried out using TEM. Figure 2c shows a typical TEM image of a $\text{CH}_3\text{NH}_3\text{PbI}_3$ nanowire with width of ca. 500 nm and its single-crystal character can be determined by the selected area electron diffraction (SAED) pattern (Inset in Figure 2c). According to the SAED analysis, it can be seen that the $\text{CH}_3\text{NH}_3\text{PbI}_3$ nanowire grow along the [100] direction and closed by the (001) and (00 $\bar{1}$) facet on the top and bottom sides. Furthermore, HRTEM image provides additional evidence for the crystallinity and growth characteristics of $\text{CH}_3\text{NH}_3\text{PbI}_3$ nanowire. Figure 2d shows the nanowire with clear lattice fringes of 0.312 and 0.440 nm corresponding to the (220) and (200) lattice spacing of tetragonal $\text{CH}_3\text{NH}_3\text{PbI}_3$ crystal. Based on the observed fringes, the white square drawn in the Figure 2d shows the four relevant crystal

facet being perpendicular to c axis of the $\text{CH}_3\text{NH}_3\text{PbI}_3$ crystal. On the basis of above analysis, the crystalline structure of the PbI_2 and $\text{CH}_3\text{NH}_3\text{PbI}_3$ perovskite nanowires can be simulated in Figure 2e and f.

Furthermore, we also prepared the organic-inorganic perovskite using PbI_2 nanowire and $\text{CH}_3\text{NH}_3\text{Br}$, $\text{CH}_3\text{NH}_3\text{Cl}$ as precursors by the same method. Energy dispersive X-ray spectroscopy (EDX) was used to probe the elemental composition of these two samples (Figure S3). It can be concluded that Br substituted the I completely when $\text{CH}_3\text{NH}_3\text{Br}$ molecular reacts with PbI_2 nanowire, leading to the formation of $\text{CH}_3\text{NH}_3\text{PbBr}_3$. Similarly, Cl partially displaced I atoms when $\text{CH}_3\text{NH}_3\text{Cl}$ molecular inserting into PbI_2 nanowire to form perovskite $\text{CH}_3\text{NH}_3\text{PbI}_x\text{Cl}_{3-x}$. The samples $\text{CH}_3\text{NH}_3\text{PbBr}_3$ and $\text{CH}_3\text{NH}_3\text{PbI}_x\text{Cl}_{3-x}$ are also maintained as nanowire morphology (Figure S4). Moreover, we also successfully synthesized PbBr_2 nanowire on mica substrate (Figure S5), which can be converted into $\text{CH}_3\text{NH}_3\text{PbI}_x\text{Br}_{3-x}$ and $\text{CH}_3\text{NH}_3\text{PbBr}_x\text{Cl}_{3-x}$ perovskite nanowires (see Methods).

Figure 3a-c display the temperature dependent PL spectra of $\text{CH}_3\text{NH}_3\text{PbI}_3$, $\text{CH}_3\text{NH}_3\text{PbI}_x\text{Cl}_{3-x}$ and $\text{CH}_3\text{NH}_3\text{PbI}_x\text{Br}_{3-x}$, respectively. As temperature (T) is between 300 K and ~ 160 K, only one emission peak was observed, with a monotonic peak redshifts and width narrowing with the decreasing of the temperature. The photoluminescence of the perovskites can be attributed to the combination of the excited electrons in Pb $6p$ states and the hole in X ($X = \text{Cl}, \text{Br}$ and I) out p states.²⁴ The Pb-X bond distances and connectivity (corner/edge sharing) of infinitely extended PbI_6 octahedral units influences exciton energies, causing the different emission energy of these perovskites.^{6, 25} Whether the emission origin of the perovskites is due to free

exciton or free carrier is still in debate.^{14, 15} Exciton binding energy was measured or evaluated by various experimental and theoretical pathways, while a broad range of values from several to tens of meV were reported. First of all, the low stability of the materials may introduce additional error in widely-used optical measurements. Secondly, since the materials are hybrid organic-inorganic semiconductor, the previous theory or experimental techniques based on traditional inorganic semiconductor may not be sufficient to explain the observations. While, since the perovskite family shows high light harvesting and conversion efficiency, a free carrier model at room temperature is more acceptable. As T is ~ 140 - 150 K, a new emission peak with a higher energy shows up, which is due to the phase transition of the organo-lead halide perovskite and the formation of orthorhombic phase as reported previously.²⁶ When the temperature further decreases from ~ 140 - 77 K, the higher energy emission peak gains strength in intensity and monotonically shifts to longer wavelengths, whereas the lower energy emission peak become relatively weaken gradually compared to the higher energy emission peak. It can be seen that as the temperature decreases, both of the two emission peaks redshift. This ‘Varshni’ trend is often observed in lead composite semiconductors.²⁷ The photoluminescence emission energy E_g is extracted and plotted in Figure 3f. Interestingly, these three perovskites nanowires have nearly the same value of dE_g/dT either in high or low temperature crystalline phases. Figure 3d shows the temperature dependent photoluminescence spectra of $\text{CH}_3\text{NH}_3\text{PbBr}_3$ nanowires. As T decreases from 296 to 77 K, only one photoluminescence peak can be resolved with pronounced redshift, indicating the absence of phase transition. Previous X-ray diffraction (XRD) studies show that four phases can be identified for the $\text{CH}_3\text{NH}_3\text{PbBr}_3$ ($T > 236.9$ K cubic Pm3m; 155.1

$K < T < 236.9$ K tetragonal I4/mcm and 149.5 K $< T < 155.1$ K tetragonal P4/mmm; $T < 144.5$ K orthorhombic Pna21).²⁸ The mechanism needs to be further investigated. The perovskite $\text{CH}_3\text{NH}_3\text{PbBr}_x\text{Cl}_{3-x}$ exhibits a very different trend from the above four perovskites. As shown in Figure 3e, the emission from room-temperature can be deconvoluted into two individual peaks, possible due to two kinds of recombination centers. Both of the two peaks blueshift at $T > 180$ K and then redshift at $T < 160$ K. This anomalous behavior of peak shift is very similar with some alloys (*e.g.* InGaN, AlGaIn and ZnCdO) that show ‘S’-shaped variation of the photoluminescence peak energy with increasing temperature from 10 K to room temperature.^{29, 30} In general, these alloy materials have carrier localization effect, which can be ascribed to the potential fluctuation, a consequence of the inhomogeneous composition. At different temperature region, the photoluminescence shift is dominated by different factors, which causes the different shift trend at different temperature region. To observe the emission energy of these perovskite nanowires clearly, we summarized the temperature dependent emission energy in Figure 3f.

Semiconductor nanowires offer the possibility of reducing the size of devices for three-dimensional device integration and therefore are being extensively studied in the context of optoelectronic devices, such as photonic and plasmonic nanolasers and waveguides.³¹⁻³⁸ Perovskites have been suggested to be able to provide sufficient gain towards lasing and we have recently demonstrated whispering gallery mode lasing at near infrared wavelength at room temperature.^{14, 15} In nanowire morphology, a good Fabry-Pérot cavity naturally form, as such it would be meaningful to explore the Fabry-Pérot lasing in perovskites with facile tuning of wavelength, towards the design of nanoscale

optoelectronic devices operating at visible and near-infrared wavelengths. In Figure 4a, we display the PL spectra from a typical $\text{CH}_3\text{NH}_3\text{PbI}_3$ nanowire (length $\sim 10\ \mu\text{m}$ and diameter $\sim 200\ \text{nm}$) at a pumping fluence ranging from 3.6 to $15\ \mu\text{J}/\text{cm}^2$. The integrated output emission and the full width at half maximum (FWHM) over the whole spectra range as a function of pumping fluence are shown in the inset of Figure 4a, which shows the evolution from a spontaneous emission to lasing behavior. The experiment data (black points) is well fitted by two different linear parts (black line) with a knee at $P_{\text{ex}} \sim 11\ \mu\text{J}/\text{cm}^2$, which is the corresponding lasing threshold P_{th} . From the spectra measured at pump fluence above lasing threshold, the mode distance ($\Delta\lambda$) of lasing peak is around $2\ \text{nm}$, which is in good agreement with the theoretical equation $\Delta\lambda = (1/L)[(\lambda^2/2)(n - \lambda \text{dn}/\text{d}\lambda)^{-1}]$ for a Fabry-Pérot cavity. The Fabry-Pérot mode of λ ($777.0\ \text{nm}$) has a λ_{FWHM} of $\sim 1.9\ \text{nm}$, leading to a corresponding Q-factor of ~ 405 (Figure S6). Further confirming the lasing action, we note the bright field image of a single nanowire and the corresponding PL images with increasing the pump fluence (Figure 4b). When the excitation fluence is below the threshold, the entire nanowire is dim but uniform. However, above the threshold, two bright spots at the distal ends of the nanowire are observed. To investigate the lasing property dependent on temperature, we conducted the lasing actions with decreasing of the temperature from $300\ \text{K}$ to $80\ \text{K}$. It can be seen from Figure 4c, the lasing wavelength always redshifts with the decreasing of temperature; however, the lasing occurs at lower energy side ($\sim 780\ \text{nm}$) above $160\ \text{K}$ while occurs at higher energy side below $140\ \text{K}$. This behavior is consistent with the PL measurement results as shown in Figure 3a that the lasing peak positions are determined by the gain area. To expand the lasing wavelength, we have also measured the lasing behavior in

CH₃NH₃PbBr₃ and CH₃NH₃PbI_xCl_{3-x} nanowire samples. The lasing wavelength can be tuned from 777 nm to 744 nm (CH₃NH₃PbI_xCl_{3-x}) and then 551 nm (CH₃NH₃PbBr₃) (Figure 4d). Through precisely tuning the component ratio between Br and Cl (I) in CH₃NH₃PbBr_xCl_{3-x} or CH₃NH₃PbI_xBr_{3-x}, fine tuning of the lasing wavelength can be fulfilled. It should be noted that the lasing threshold for CH₃NH₃PbBr₃ (20 μJ/cm²) and CH₃NH₃PbI_xCl_{3-x} (60 μJ/cm²) is slightly larger than that (11 μJ/cm²) in CH₃NH₃PbI₃, which might be caused by the low losses in the CH₃NH₃PbI₃ for the relatively longer wavelength of emission. Time-resolved photoluminescence measurements are also performed, as shown in Figure 4e, all three curves exhibit single exponential decay. It can be seen that CH₃NH₃PbI₃ has a relatively long lifetime (~3.7 ns), while a shorter lifetime are observed in CH₃NH₃PbBr₃ (~220 ps) and CH₃NH₃PbI_xCl_{3-x} (~230 ps) nanowires. When lasing occurs in the nanowire, a very fast lifetime (~10 ps, close to the system time resolution) of CH₃NH₃PbI₃ can be observed as shown in Figure S7. From previous reports, the measured lifetime for CH₃NH₃PbI_xCl_{3-x} film is generally in nanoseconds regime. Through passivation, enhanced lifetime with the magnitude of μs is observed in the lead halide perovskite.³⁹ A high density of defects states always caused a relatively short lifetime, where a large degree of electronic disorder exhibits. In our nanowire structured samples, due to the special morphology which is not compatible with its intrinsic lattice structure and large surface to volume ratio, it is reasonable that short lifetimes are observed in our system. A latest work on perovskite nanowire laser based on solution method has been published and it exhibit a low threshold and high quality factor;⁴⁰ however, our work provide a new and versatile method for synthesizing lead

halide perovskite nanowire with good crystal quality, which provides us the insightful optical investigations of the perovskite nanowires.

In conclusion, organic-based lead halide perovskite nanowires with single crystalline structure were prepared successfully by a vapor phase synthesis. Using the perovskite nanowires, we have realized room-temperature visible and near-infrared solid-state nanowire lasers. Their naturally formed high-quality Fabry-Pérot mode cavities and long diffusion lengths provide adequate gain and efficient optical feedback for low-threshold optically pumped lasing. Our research will create a new platform for exploiting nanoscale optical, electronic and optoelectronic devices on the basis of free-standing organic-inorganic perovskite nanowire with high crystal quality.

METHODS:

Synthesis of PbI₂/PbBr₂ nanowire: PbI₂ powder was used as a single source put into a quartz tube in a single-zone furnace (Lindberg/Blue MTF55035C-1). The silicon substrate with oxide thickness of 285 nm (1 cm × 1 cm) was pre-cleaned with acetone, ethanol and water, and placed in the downstream region inside the quartz tube. The quartz tube was first evacuated to a base pressure of 40 mTorr, followed by a 30 sccm flow of high purity H₂/Ar (5 vol %/95 vol %). After flowing of the gas for 30 min to eliminate the residual air, the experiment could start. The temperature and pressure inside the quartz tube were set and stabilized to 380 °C and 200 Torr. The synthesis was operated for 15 minutes and the furnace was allowed to cool down naturally to ambient temperature. For synthesis of PbBr₂, mica substrate (1 cm × 3 cm) was placed in the downstream region inside the quartz tube. The temperature and pressure inside the quartz tube were set and stabilized to 350 °C and 50 Torr.

Conversion of lead halides to perovskites: The conversions were carried out using the same CVD system. Methyl ammonium halides $\text{CH}_3\text{NH}_3\text{X}$ ($\text{X} = \text{I}, \text{Br}$ or Cl) synthesized by a solution method (detailed synthesis method can be found somewhere else)²⁴ were used as a source and placed in the center of the quartz tube while silicon wafer hosting lead halide nanowires was placed around 5 cm away from the center in the downstream region. The quartz tube was first evacuated to a base pressure of 40 mTorr, followed by a 30 sccm flow of high purity N_2 gas. The temperature and pressure was stabilized at 120 °C and 50 Torr for 1 hour for $\text{CH}_3\text{NH}_3\text{I}$ and $\text{CH}_3\text{NH}_3\text{Br}$, and the temperature was kept at 100 °C for $\text{CH}_3\text{NH}_3\text{Cl}$.

Characterizations: The structure of the as-grown samples were characterized using an optical microscope (Olympus BX51), AFM (Veeco Dimension V) in the tapping mode, field-emission scanning electron microscopy (FE-SEM, JEOL JSM-7001F) and transmission electron microscopy with energy-dispersive X-ray spectroscopy (TEM; JEM 2100F, 200 kV and ZEISS, 120 kV). Temperature dependent PL spectra were measured through a micro-Raman spectrometer (Horiba-JY T64000) with a single-grating setup. A series of laser lines 325 nm and 473 nm (solid state laser) were used as the excitation sources. The backscattered signal was collected through a 20×(UV) and 100×(VIS) objective and recorded by a liquid nitrogen cooled charge coupled device detector.

Lasing measurement and time-resolved photoluminescence spectroscopy: The excitation pulse (400 nm) was generated by frequency doubling the 800 nm output (with a BBO crystal) from the Coherent Libra regenerative amplifier (50 fs, 1 kHz, 800 nm) which is seeded by a Coherent Vitesse oscillator (50 fs, 80 MHz). The pump laser source is introduced into a microscope (Nikon LV100) and focused onto samples via a 20×

objective (Nikon, numerical aperture: 0.4). To obtain sufficient energy injection, the laser spot is focused to $\sim 40\text{ }\mu\text{m}$ in diameter. The backscattered emission is collected by the same objective. The emission signal was then analyzed by a spectrometer (Princeton Instrument SP2300i) equipped with a TE-cooled charge coupled device detector. For time-resolved photoluminescence spectra of single nanowire, a Coherent Mira 900 (120 fs, 76MHz) was used as the pump laser source. The output 800 nm wavelength pulse was double frequency by a BBO crystal to 400 nm and the PL emission was collected in a standard backscattering geometry and dispersed by a 0.25 m DK240 spectrometer with 150 g/mm grating. The emission was time-resolved using an Optronic Streak Camera system that has an ultimate temporal resolution of $\sim 10\text{ ps}$.

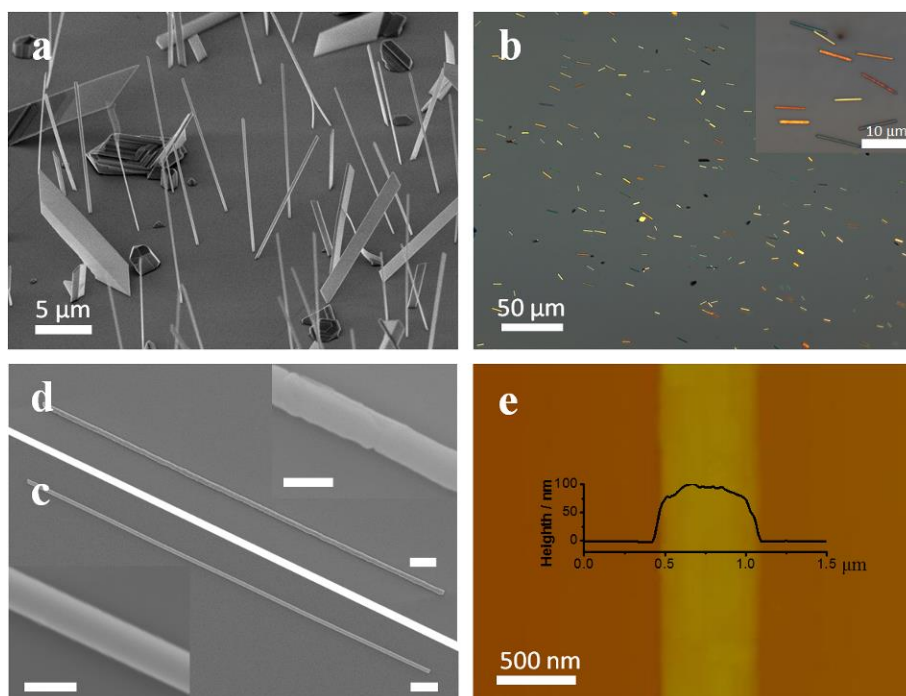


Figure 1. (a) SEM image of PbI₂ nanowires grown on silicon substrate. (b) Optical microscopy image of CH₃NH₃PbI₃ nanowires on silicon substrate. Inset in (b) is the magnified image. SEM images of PbI₂ nanowire (c) and its corresponding conversion product CH₃NH₃PbI₃ nanowire (d). Insets in (c) and (d) are their corresponding magnified SEM images. Scale bars in (c, d) and their insets are 2 μm and 500 nm, respectively. (e) AFM image of the CH₃NH₃PbI₃ nanowire lies flat on silicon substrate.

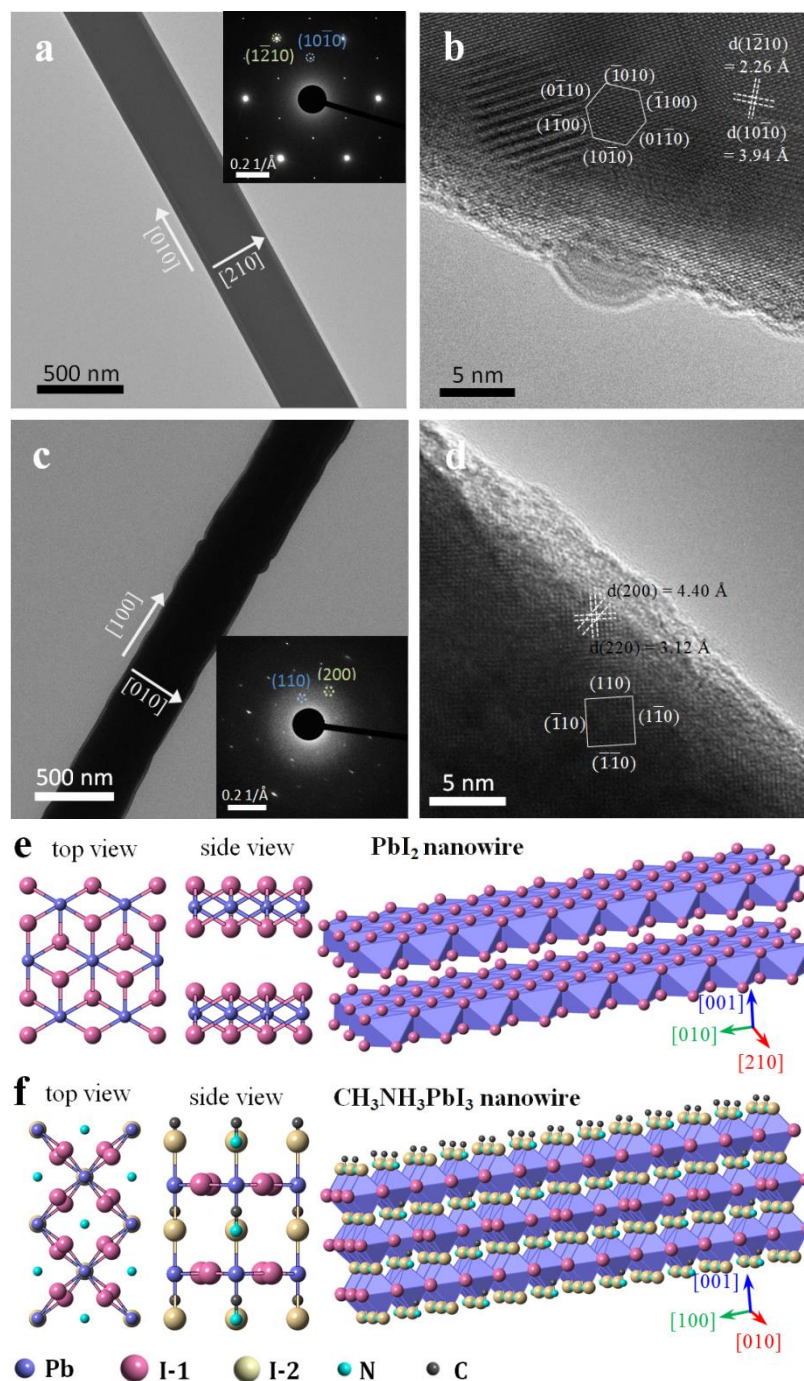


Figure 2. TEM and HRTEM images of PbI_2 nanowire (a, b) and $\text{CH}_3\text{NH}_3\text{PbI}_3$ nanowire (c, d). Insets in (a) and (c) are their corresponding SAED patterns. Structure simulation images of PbI_2 nanowire (e) and $\text{CH}_3\text{NH}_3\text{PbI}_3$ nanowire (f).

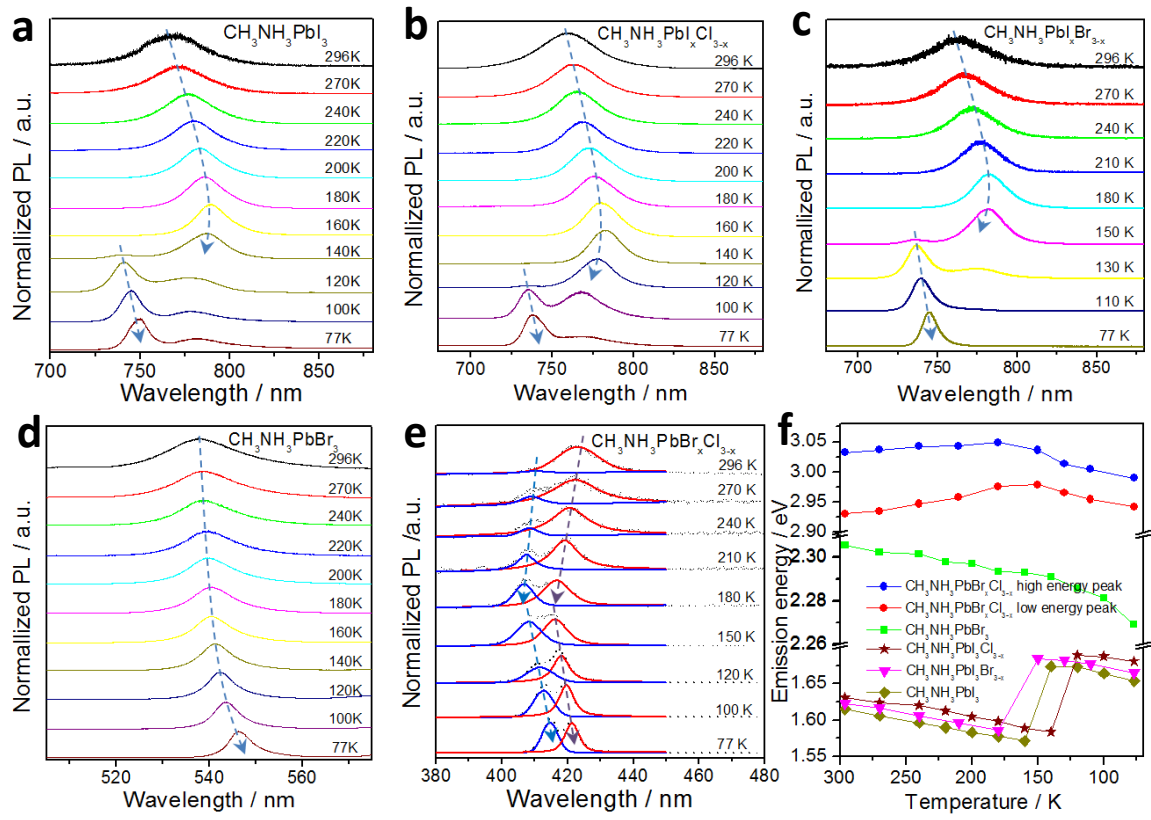


Figure 3. (a-e) Temperature dependent PL spectra taken from 296 K to 77 K; for clarity, the intensities of the spectra are normalized. (f) Temperature dependent emission energy from 296 K to 77 K.

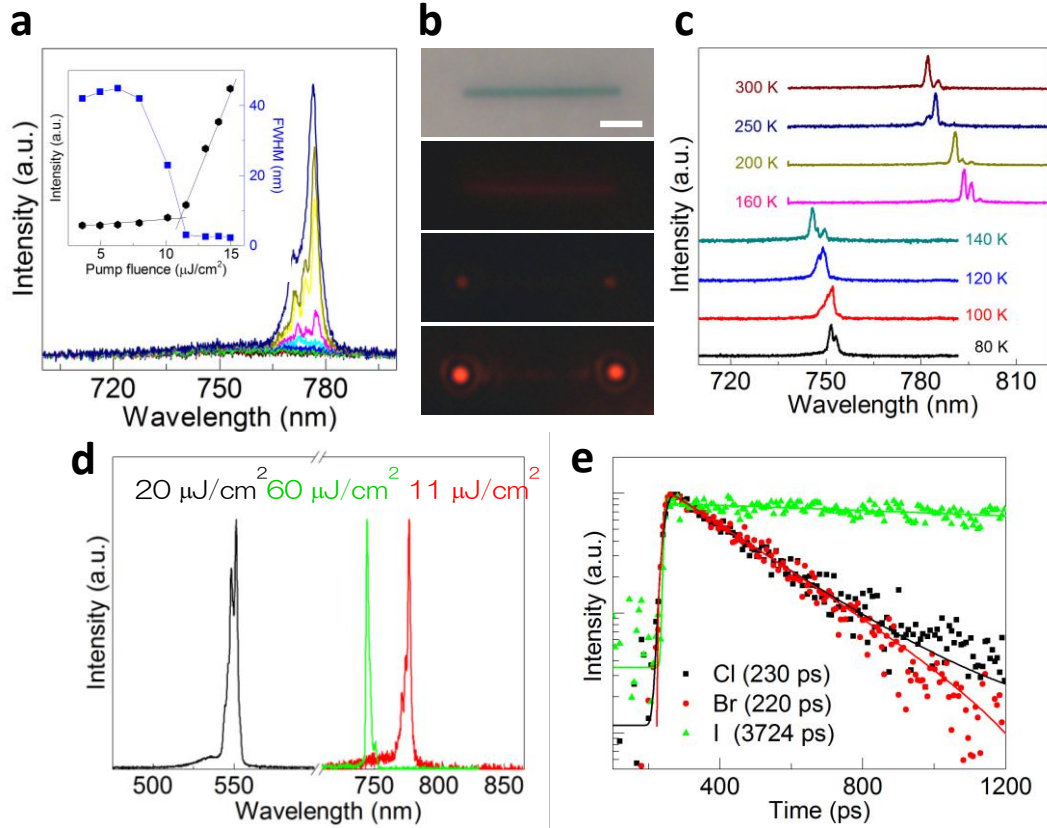


Figure 4. (a) The evolution from spontaneous emission to lasing (Fabry-Pérot mode) in a typical $\text{CH}_3\text{NH}_3\text{PbI}_3$ nanowire. The pumping fluences range from $3.6 \mu\text{J}/\text{cm}^2$ to $15 \mu\text{J}/\text{cm}^2$. Inset is integrated output emission (P_{out}) and the FWHM over the whole spectra range as a function of pumping fluence (P_{ex}). The experiment data (black points) is well fitted by distinguished functions (black line) with a knee at $P_{\text{ex}} \sim 11 \mu\text{J}/\text{cm}^2$ (lasing threshold P_{th}). $\lambda_{\text{FWHM}} \sim 1.9 \text{ nm}$ for Fabry-Pérot mode $\lambda = 777.0 \text{ nm}$ and the corresponding Q-factor is ~ 405 (Figure S6). (b) The bright filed image of a single $\text{CH}_3\text{NH}_3\text{PbI}_3$ nanowire and the corresponding PL images with increasing the pump fluences (from below the threshold to above the threshold, fake color, the scale bar is $5 \mu\text{m}$). (c) Lasing behavior of single $\text{CH}_3\text{NH}_3\text{PbI}_3$ nanowire at different temperatures. (d) Lasing spectra of $\text{CH}_3\text{NH}_3\text{PbI}_3$, $\text{CH}_3\text{NH}_3\text{PbBr}_3$ and $\text{CH}_3\text{NH}_3\text{PbI}_x\text{Cl}_{3-x}$. For $\text{CH}_3\text{NH}_3\text{PbBr}_3$, $P_{\text{ex}} = 20 \mu\text{J}/\text{cm}^2$, $\lambda_{\text{FWHM}} \sim 2.0 \text{ nm}$ for Fabry-Pérot mode $\lambda = 551.3 \text{ nm}$ and the corresponding Q-factor is ~ 225 . For $\text{CH}_3\text{NH}_3\text{PbI}_x\text{Cl}_{3-x}$, $P_{\text{ex}} = 60 \mu\text{J}/\text{cm}^2$, $\lambda_{\text{FWHM}} \sim 1.6 \text{ nm}$ for Fabry-Pérot mode $\lambda = 744.4 \text{ nm}$ and the corresponding Q-factor is ~ 372 (Figure

S6). (e) The photoluminescence decay profile of individual $\text{CH}_3\text{NH}_3\text{PbI}_3$, $\text{CH}_3\text{NH}_3\text{PbBr}_3$ and $\text{CH}_3\text{NH}_3\text{PbI}_x\text{Cl}_{3-x}$ nanowire.

Supporting Information

Additional SEM, TEM, EDX analysis and lasing spectra can be found in the supporting information. This material is available free of charge via the Internet at <http://pubs.acs.org>.

Author Contributions

J.X. and Q.X. conceived the idea and designed the experiment. J.X. prepared the samples and performed the SEM measurements. Q.Z. performed photoluminescence spectroscopy measurements. X.F.L. and T.C.S. conducted the lasing and time-resolved photoluminescence measurement. Y.W.Y. performed TEM measurements. C.S. performed AFM measurements. All the authors co-wrote the manuscript. J.X. and X.F.L. contribute equally to this work.

Notes

The authors declare no competing financial interest.

ACKNOWLEDGMENT

This work was mainly supported by Singapore Ministry of Education via an AcRF Tier2 grant (MOE2011-T2-2-051). In addition, the author Q.X. also gratefully thanks the strong support from Singapore National Research Foundation through an Investigatorship Grant (NRF-NRFI2015-03) and a Competitive Research Program (NRF-CRP-6-2010-2). This work is supported in part by the A*Star Science and Engineering Research Council Public Sector Funding (122-PSF-0011). Q.X. and T.C.S also acknowledge the funding of

this research programme/project by the National Research Foundation (NRF), Prime Minister's Office, Singapore under its Campus for Research Excellence and Technological Enterprise (CREATE) programme.

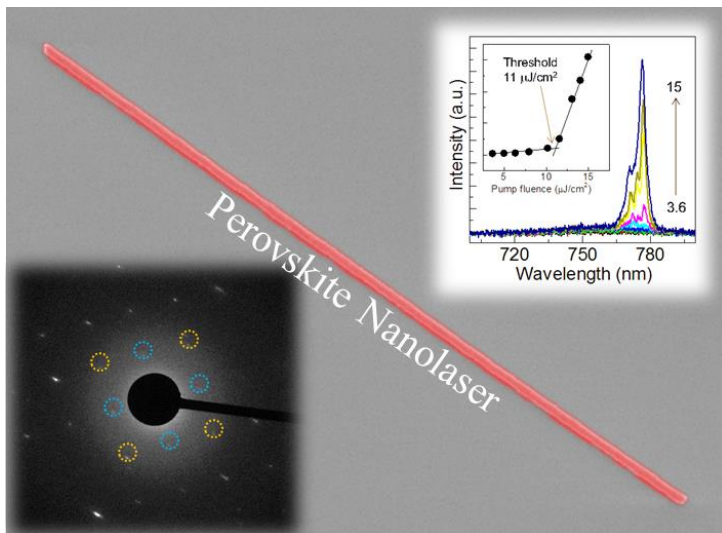
REFERENCES

1. Stoumpos, C. C.; Malliakas, C. D.; Kanatzidis, M. G. *Inorg. Chem.* **2013**, 52, (15), 9019-9038.
2. Mitzi, D. B. *J. Mater. Chem.* **2004**, 14, (15), 2355-2365.
3. Cheng, Z.; Lin, J. *CrystEngComm* **2010**, 12, (10), 2646-2662.
4. Stranks, S. D.; Eperon, G. E.; Grancini, G.; Menelaou, C.; Alcocer, M. J. P.; Leijtens, T.; Herz, L. M.; Petrozza, A.; Snaith, H. J. *Science* **2013**, 342, (6156), 341-344.
5. Baikie, T.; Fang, Y.; Kadro, J. M.; Schreyer, M.; Wei, F.; Mhaisalkar, S. G.; Graetzel, M.; White, T. J. *J. Mater. Chem. A* **2013**, 1, (18), 5628-5641.
6. Ahmad, S.; Prakash, G. V. *J. Nanophotonics* **2014**, 8, (1), 083892.
7. Dong, Q.; Fang, Y.; Shao, Y.; Mulligan, P.; Qiu, J.; Cao, L.; Huang, J. *Science* **2015**, 347, (6225), 967-970.
8. Lee, M. M.; Teuscher, J.; Miyasaka, T.; Murakami, T. N.; Snaith, H. J. *Science* **2012**, 338, (6107), 643-647.
9. Liu, M.; Johnston, M. B.; Snaith, H. J. *Nature* **2013**, 501, (7467), 395-398.
10. Kojima, A.; Teshima, K.; Shirai, Y.; Miyasaka, T. *J. Am. Chem. Soc.* **2009**, 131, (17), 6050-6051.
11. Zhou, H.; Chen, Q.; Li, G.; Luo, S.; Song, T.-b.; Duan, H.-S.; Hong, Z.; You, J.; Liu, Y.; Yang, Y. *Science* **2014**, 345, (6196), 542-546.
12. Burschka, J.; Pellet, N.; Moon, S.-J.; Humphry-Baker, R.; Gao, P.; Nazeeruddin, M. K.; Gratzel, M. *Nature* **2013**, 499, (7458), 316-319.
13. http://www.nrel.gov/ncpv/images/efficiency_chart.jpg.
14. Xing, G.; Mathews, N.; Lim, S. S.; Yantara, N.; Liu, X.; Sabba, D.; Grätzel, M.; Mhaisalkar, S.; Sum, T. C. *Nat. Mater.* **2014**, 13, (5), 476-480.
15. Zhang, Q.; Ha, S. T.; Liu, X.; Sum, T. C.; Xiong, Q. *Nano Lett.* **2014**, 14, (10), 5995-6001.
16. Tan, Z.-K.; Moghaddam, R. S.; Lai, M. L.; Docampo, P.; Higler, R.; Deschler, F.; Price, M.; Sadhanala, A.; Pazos, L. M.; Credgington, D.; Hanusch, F.; Bein, T.; Snaith, H. J.; Friend, R. H. *Nat. Nanotechnol.* **2014**, 9, (9), 687-692.
17. Kagan, C. R.; Mitzi, D. B.; Dimitrakopoulos, C. D. *Science* **1999**, 286, (5441), 945-947.

18. Lee, Y.; Kwon, J.; Hwang, E.; Ra, C.-H.; Yoo, W. J.; Ahn, J.-H.; Park, J. H.; Cho, J. H. *Adv. Mater.* **2014**, 27, (1), 41-46.
19. Era, M.; Morimoto, S.; Tsutsui, T.; Saito, S. *Appl. Phys. Lett.* **1994**, 65, (6), 676-678.
20. Horváth, E.; Spina, M.; Szekrényes, Z.; Kamarás, K.; Gaal, R.; Gachet, D.; Forró, L. *Nano Lett.* **2014**, 14, (12), 6761-6766.
21. Mitzi, D. B.; Dimitrakopoulos, C. D.; Kosbar, L. L. *Chem. Mater.* **2001**, 13, (10), 3728-3740.
22. Liu, X.; Ha, S. T.; Zhang, Q.; de la Mata, M.; Magen, C.; Arbiol, J.; Sum, T. C.; Xiong, Q. *ACS Nano* **2015**, 9, (1), 687-695.
23. Im, J.-H.; Luo, J.; Franckevičius, M.; Pellet, N.; Gao, P.; Moehl, T.; Zakeeruddin, S. M.; Nazeeruddin, M. K.; Grätzel, M.; Park, N.-G. *Nano Lett.* **2015**, 15, (3), 2120-2126.
24. Ha, S. T.; Liu, X.; Zhang, Q.; Giovanni, D.; Sum, T. C.; Xiong, Q. *Adv. Opt. Mater.* **2014**, 2, (9), 838-844.
25. Wang, Y.; Gould, T.; Dobson, J. F.; Zhang, H.; Yang, H.; Yao, X.; Zhao, H. *PCCP* **2014**, 16, (4), 1424-1429.
26. D’Innocenzo, V.; Grancini, G.; Alcocer, M. J. P.; Kandada, A. R. S.; Stranks, S. D.; Lee, M. M.; Lanzani, G.; Snaith, H. J.; Petrozza, A. *Nat. Commun.* **2014**, 5, 3586.
27. Ashcroft, N. W.; Mermin, N. D. *Solid State Physics* (Holt Rinehart & Winston, 1976).
28. Poglitsch, A.; Weber, D. *J. Chem. Phys.* **1987**, 87, (11), 6373.
29. Schenk, H. P. D.; Leroux, M.; de Mierry, P. *J. Appl. Phys.* **2000**, 88, (3), 1525-1534.
30. Yang, W. F.; Xie, Y. N.; Pan, Z. Y.; Hong, M. H.; Wu, Z. Y.; Wong, L. M.; Wang, S. J.; Wang, C. F.; Lee, A. Y. S.; Gong, H. *EPL (Europhysics Letters)* **2012**, 99, (2), 27003.
31. Huang, M. H.; Mao, S.; Feick, H.; Yan, H.; Wu, Y.; Kind, H.; Weber, E.; Russo, R.; Yang, P. *Science* **2001**, 292, (5523), 1897-1899.
32. Oulton, R. F.; Sorger, V. J.; Zentgraf, T.; Ma, R.-M.; Gladden, C.; Dai, L.; Bartal, G.; Zhang, X. *Nature* **2009**, 461, (7264), 629-632.
33. Zhang, Q.; Li, G.; Liu, X.; Qian, F.; Li, Y.; Sum, T. C.; Lieber, C. M.; Xiong, Q. *Nat. Commun.* **2014**, 5, 4953.

34. Zhang, C.; Zou, C.-L.; Yan, Y.; Hao, R.; Sun, F.-W.; Han, Z.-F.; Zhao, Y. S.; Yao, J. *J. Am. Chem. Soc.* **2011**, 133, (19), 7276-7279.
35. Guo, P.; Zhuang, X.; Xu, J.; Zhang, Q.; Hu, W.; Zhu, X.; Wang, X.; Wan, Q.; He, P.; Zhou, H.; Pan, A. *Nano Lett.* **2013**, 13, (3), 1251-1256.
36. Pan, A.; Zhou, W.; Leong, E. S. P.; Liu, R.; Chin, A. H.; Zou, B.; Ning, C. Z. *Nano Lett.* **2009**, 9, (2), 784-788.
37. Piccione, B.; Cho, C.-H.; van Vugt, L. K.; Agarwal, R. *Nat. Nanotechnol.* **2012**, 7, (10), 640-645.
38. Saxena, D.; Mokkaapati, S.; Jagadish, C. *IEEE Photonics J.* **2012**, 4, (2), 582-585.
39. Leijtens, T.; Stranks, S. D.; Eperon, G. E.; Lindblad, R.; Johansson, E. M. J.; McPherson, I. J.; Rensmo, H.; Ball, J. M.; Lee, M. M.; Snaith, H. J. *ACS Nano* **2014**, 8, (7), 7147-7155.
40. Zhu, H.; Fu, Y.; Meng, F.; Wu, X.; Gong, Z.; Ding, Q.; Gustafsson, M. V.; Trinh, M. T.; Jin, S.; Zhu, X. Y. *Nat. Mater.* **2015**, 14, (6), 636-642.

Table of Contents Graphic



Supporting Information

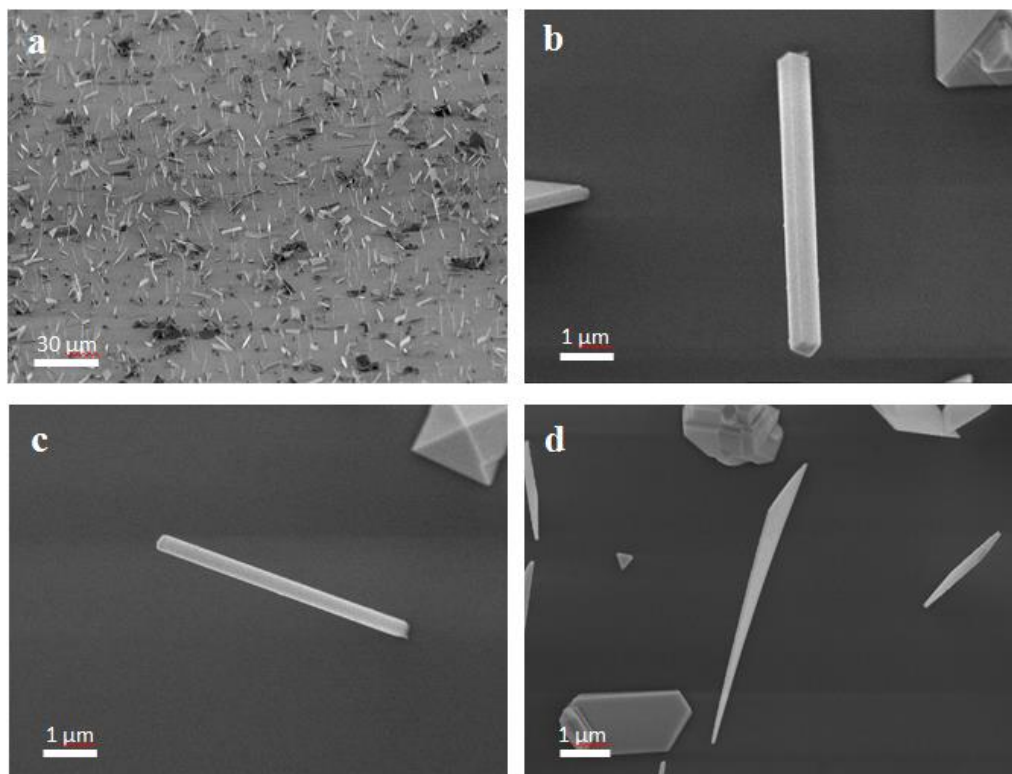


Figure S1. SEM images of PbI₂ grown on silicon substrate.

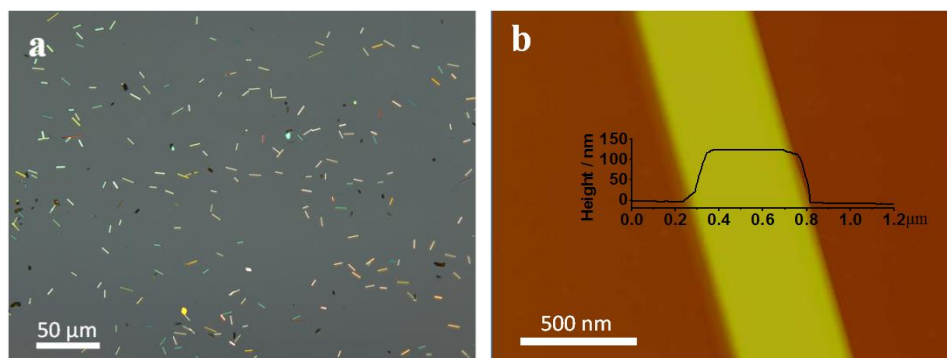


Figure S2. Optical microscope (a) and AFM (b) images of PbI₂ nanowire transferred onto silicon substrate.

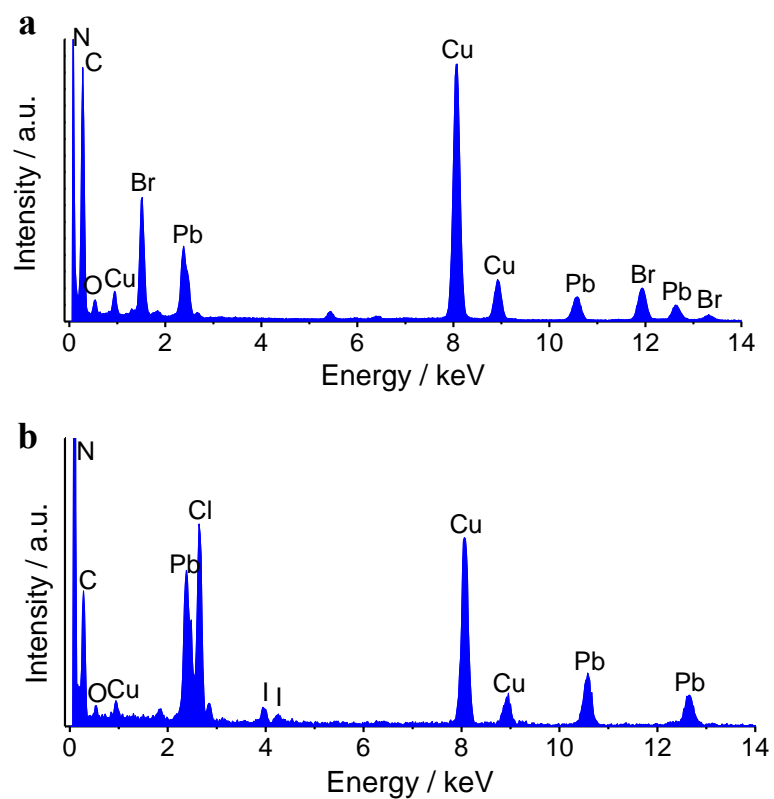


Figure S3. EDX analysis of samples $\text{CH}_3\text{NH}_3\text{PbBr}_3$ (a) and $\text{CH}_3\text{NH}_3\text{PbI}_x\text{Cl}_{3-x}$ (b).

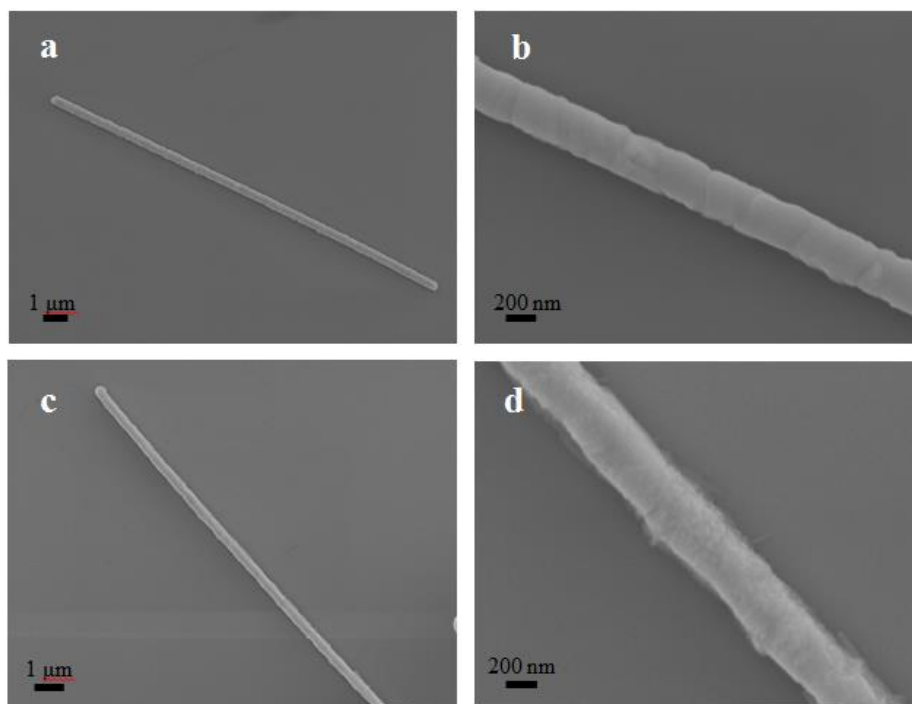


Figure S4. SEM images of $\text{CH}_3\text{NH}_3\text{PbBr}_3$ (a, b) and $\text{CH}_3\text{NH}_3\text{PbI}_x\text{Cl}_{3-x}$ (c, d).

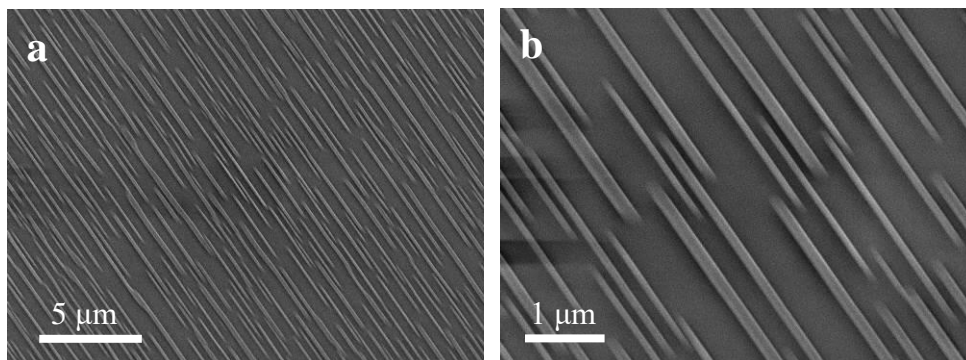


Figure S5. SEM images of as-grown PbBr_2 nanowires on mica substrate.

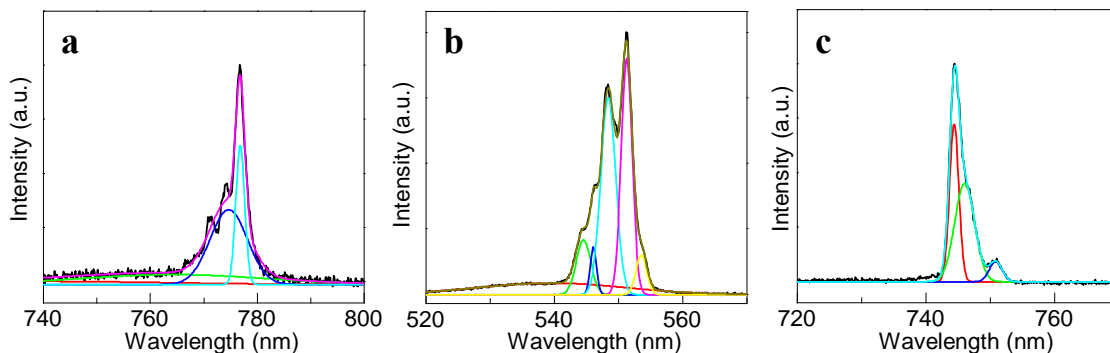


Figure S6. Lasing spectra of $\text{CH}_3\text{NH}_3\text{PbI}_3$ (a), $\text{CH}_3\text{NH}_3\text{PbBr}_3$ (b) and $\text{CH}_3\text{NH}_3\text{PbI}_x\text{Cl}_{3-x}$ (c). In figure a, we should fit the three sharp peaks at around lasing peak instead of one broad peak and a sharp peak.

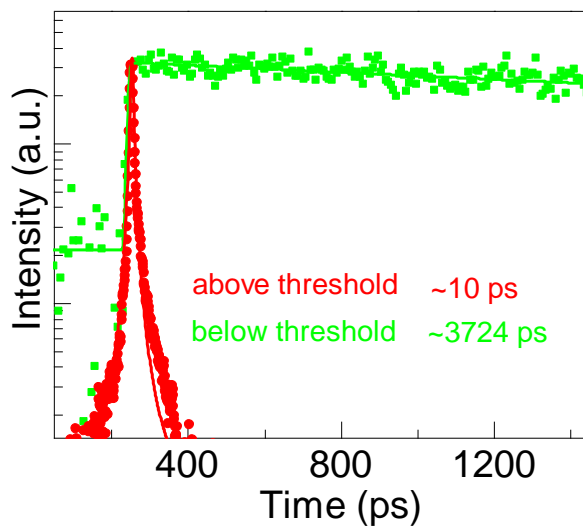


Figure S7. Time-resolved photoluminescence spectra of single $\text{CH}_3\text{NH}_3\text{PbI}_3$ nanowire under the laser power below and above the threshold.